Ab initio insight into the formation of small polarons: A study across four metal peroxides

Shuaishuai Yuan ,* Zi Wang , Maximilian L. F. Baron , and Kirk H. Bevan
Division of Materials Engineering, Faculty of Engineering, McGill University, Montréal, Québec, Canada H3A 0C5

(Received 16 August 2019; revised manuscript received 8 October 2019; published 6 November 2019)

In this *ab initio* study, we investigate the initial stages of small polaron formation across four metal peroxides. By separating out electronic and lattice energy contributions to the formation of electron polarons, we find both large and small formation barriers directly correlated with an electronic relaxation delay. Further analysis of the electronic structure evolution during polaron formation, within the constraints set by the generalized form of Koopmans' theorem, reveals that hybridization between the polaron anchoring orbital and the conduction band minimum determines the electronic relaxation delay. This hybridization physics is shown to play a dominant role in the magnitude of a polaron formation barrier and the adiabaticity of polaron charge localization. Weaker hybridization is correlated with larger more diabatic formation barriers, while stronger hybridization is correlated with smaller more adiabatic formation barriers. These *ab initio* insights may lead to new approaches towards tailoring the formation of small polarons in energy and electronic materials.

DOI: 10.1103/PhysRevB.100.205201

I. INTRODUCTION

Polaron formation is the process by which free electrons (or holes) in a material find a lower energy localized state by distorting their surrounding host lattice. Since polaron formation involves changes in both electronic and atomic coordinates, it can have a significant impact upon various material properties such as conductivity, optical absorption, and even chemical reactivity [1]. Material properties resulting from polaron formation have been well established by many experimental methods, including: DC conductivity, Seebeck, electron paramagnetic resonance, Mössbauer spectroscopy, scanning tunneling microscopy, transient absorption, and time-resolved THz conductivity measurements [2–7]. The existence of polarons was first postulated by Landau in 1933 in a short note and then further developed by Pekar and Rashba [8–10]. In the past half-century other researchers also have contributed significantly to the development of polaron theories, as summarized in Refs. [11–14]. With the development of *ab initio* electronic structure methods, polarons have been explored from first principles in numerous materials [15–25]. *Ab initio* studies have predominantly focused on studying stabilized small polaron states and their hopping physics, which are primarily localized within a lattice constant or so [15–23], while less investigation has been devoted to the equally important process of polaron formation [13,26–29]. In this work we provide an extensive *ab initio* exploration of the physics governing the formation of small polarons [14,29].

Small polaron formation is illustrated in Fig. 1(a), whereby an electron injected into a material is initially delocalized at the conduction band minimum (CBM) delineated by ε_C. Subsequently, through electron-lattice interactions a carrier is self-trapped to form a polaron state ε_P within the band gap (ε_G). This single-particle perspective is complemented by the total energy description of small polaron formation given in Fig. 1(b), which was first discussed in this manner by Mott and Stoneham [29]. In the total energy Mott-Stoneham picture, the transition between the free electron and the polaron configurations follows a polaron formation energy pathway E_{POL} [illustrated in black in Fig. 1(b)], which may or may not exhibit an activation barrier E_A to small polaron formation. Other pioneering early theoretical studies also explored the nature of the barrier between the free delocalized electron state and the localized polaron state [13,26–28]. More recent theoretical research has provided further support for the existence of the polaron formation barrier [30,31]. First-principles calculations have also predicted small polaron formation barriers across a wide range of materials [32,33]. There has also been success in observing polaron formation barriers experimentally through ultrafast spectroscopic measurements [34–36].

Within the Mott-Stoneham picture, the formation barrier magnitude is determined through competition between two energy terms: the strain penalty E_{LAT} imposed by the polaron on the crystal lattice [illustrated in green in Fig. 1(b)]; and the energy minimization resulting from the lowering of the electronic energy E_{EL} of the polaron forming carrier [illustrated in red in Fig. 1(b)] [17,37–39]. Formally, these contributions may be written as

$$E_{\mathrm{POL}} = E_{\mathrm{LAT}} + E_{\mathrm{EL}}. \quad (1)$$

The polaron strain penalty (E_{LAT}) invariably rises parabolically with the polaron distortion coordinate (x) [29,32]. However, E_{EL} remains flat while the carrier remains delocalized at the CBM (ε_C); it only begins to lower at distortion coordinate x_A when the electron transitions from the CBM to a localized state within the band gap. This physics is illustrated in Figs. 1(a) and 1(b). Thus, the magnitude of the polaron formation barrier is primarily determined by the electronic relaxation delay (x_A) at which the electron begins to transition from the CBM to a localized polaron state in the band gap. If $x_A \approx 0$, then there will be a negligible polaron formation barrier. Conversely, if x_A is large, then there will be a large

*Corresponding author: shuaishuai.yuan@mail.mcgill.ca

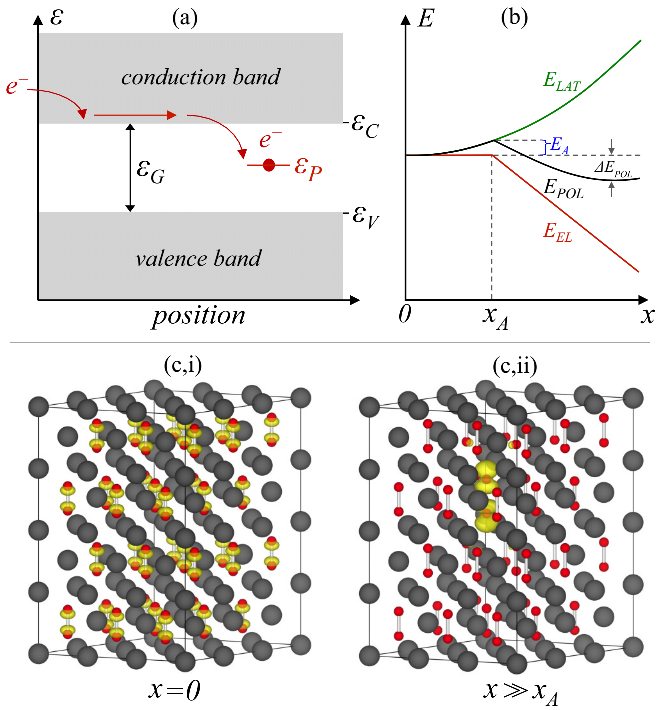

FIG. 1. (a) Schematic of small polaron formation after electron injection in the *single-particle picture*. (b) The Mott-Stoneham small polaron formation model [29] in the *total energy picture*. The polaron formation barrier (E_A) is indicated at the lattice distortion coordinate x_A, where $E_{\rm EL}$ begins to drop. (c,i) Free electron in the Li_2O_2 conduction band without any lattice distortion ($x = 0$). (c,ii) Trapped electron in Li_2O_2 well after crossing the formation barrier at x_A. The red balls represent O atoms and the black balls represent Li atoms. The electron density is shown in yellow.

polaron formation barrier. Herein, our focus is on examining the physical factors that determine the magnitude of x_A from first principles and thereby the magnitude of the formation barrier (E_A) exhibited by small polarons [32,33].

To this end we have chosen to study small polaron formation across four similar metal peroxides (Li_2O_2, Na_2O_2, K_2O_2, and BaO_2) which exhibit varying electron relaxation lengths (x_A) and corresponding formation barriers (E_A). These peroxides serve as a convenient model system for exploring the general physics of polaron formation, as they all exhibit rather simple polaron distortions dominated by the stretching of a single peroxide dimer. The nature of polaron formation in these peroxides is shown in Fig. 1(c), where delocalized and polaron electron states are shown for Li_2O_2 in Figs. 1(c,i) and 1(c,ii), respectively. By carefully analyzing electronic structure changes during the polaron formation process in this family of materials, we have found that the degree of orbital hybridization between the CBM and the polaron state dramatically impacts upon the magnitude of E_A. It is shown that strong hybridization between the CBM and polaron state results in a small adiabatic polaron formation barrier (with a negligible electronic relaxation delay, $x_A \approx 0$), while weak hybridization between the CBM and polaron state is shown to result in a much larger and more nonadiabatic (diabatic) polaron formation barrier (with a substantial electronic relaxation delay x_A).

This marks a significant *ab initio* departure from the simplified potential well model of small polaron formation first postulated by Mott and Stoneham [29]; whereby the potential well trapping the polaron state, not being a Coulomb type, can only trap a carrier if there is a finite distortion value (x_A). This is argued because, in three dimensions, the potential well has to reach a certain width and depth in order to pull a carrier below ε_C. However, the *ab initio* results presented here argue that the degree of hybridization between the small polaron state and the CBM is the primary physical characteristic which determines the magnitude of E_A (and correspondingly the extent of x_A). In general, our work seeks to more deeply explore the physical origins of large and small polaron formation barriers, which may provide further guidance towards engineering polaron properties inside materials [32].

The remainder of this work is organized as follows. The computational details of this work are described in Sec. II. Then we present our *ab initio* results in Sec. III. We begin by examining the undistorted lattice and electronic structures of the four selected metal peroxides in Sec. III A. The polaron formation barriers and corresponding energetic contributions of each material are then discussed in Sec. III B. Subsequently, the single-particle electronic structure evolution during polaron formation is explored in Secs. III C through III E, which presents the key physics connecting orbital hybridization with the eventual polaron formation barrier. In Sec. IV we provide a detailed discussion of the polaron physics and its more general implications. Finally, in Sec. V we present our conclusions.

II. COMPUTATIONAL METHODS

All calculations were performed within the Vienna *ab initio* simulation package (VASP) [40–43], utilizing the Heyd-Scuseria-Ernzerhof hybrid functional (HSE06) [44,45] and projector augmented wave (PAW) potentials [46,47] of the form: Li($1s^2 2s^1$), Na($2p^6 3s^1$), K($3s^2 3p^6 4s^1$), Ba($5s^2 5p^6 6s^2$), and O($2s^2 2p^4$). The initial structures of the four metal peroxides under investigation were obtained from the Materials Project [48]. These structures were then further relaxed until all interatomic forces were converged to less than 0.01 eV/Å using the HSE06 functional with a default mixing parameter of $\alpha = 0.25$.

The electronic structure of each material was calculated utilizing the HSE06 functional with the following mixing parameter values: $\alpha = 0.34$ for Li_2O_2, $\alpha = 0.37$ for Na_2O_2, $\alpha = 0.35$ for K_2O_2, and $\alpha = 0.28$ for BaO_2. These separate mixing parameters were carefully optimized for each material to fulfill the generalized form of Koopmans' theorem [49–51]. This was done in order to minimize self-interaction errors within HSE06, further details can be found in the Supplemental Material [52] to this work. To substantially reduce the computational cost due to our utilization of HSE06, all band structure results were computed through a non-self-consistent approach using additional high symmetry k points with zero weight in the overall total energy computation [53]. The high symmetry k points for Li_2O_2, Na_2O_2, K_2O_2, and BaO_2 were taken from the Brillouin zones provided in Ref. [54]. Gaussian smearing of 0.01 eV was used in all electronic structure calculations but its value was increased to 0.05 eV for all

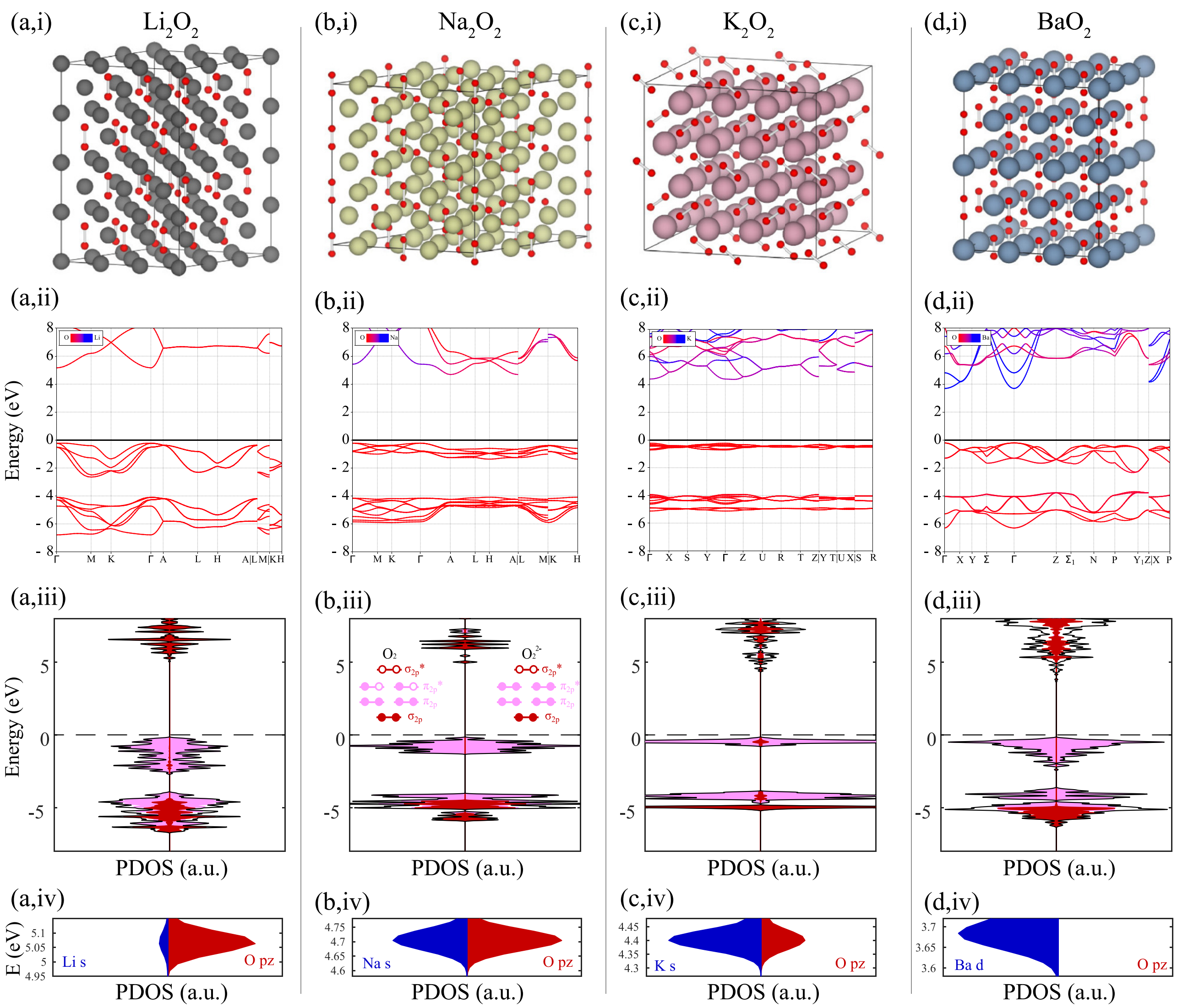

FIG. 2. Crystal structures illustrated through supercells of (a,i) Li_2O_2, (b,i) Na_2O_2, (c,i) K_2O_2, and (d,i) BaO_2. The red balls represent oxygen atoms. The black, yellow, purple, and blue balls represent Li, Na, K, and Ba, respectively. Electronic band structures of the four metal peroxides are provided in (a,ii) through to (d,ii). Contribution from metal atoms and oxygen atoms are in blue and red, respectively. Spin-polarized projected density of states (PDOS) of the four metal peroxides are given in (a,iii) through (d,iii). Projected contributions from oxygen p_z orbitals are given in red, while those from oxygen p_x and p_y orbitals are given in pink. The total DOS is plotted in black. Zoomed-in PDOS composition of the CBM for each material is given in (a,iv) through (d,iv); these are not spin-polarized plots, projected s or d orbitals of metal cations are plotted on the right and projected p_z orbitals of O atoms are plotted on the left of each figure to illustrate their relative magnitudes at the CBM.

density of states plots. Additionally, all calculations were spin polarized.

For our polaron formation calculations, the following supercells were used: $3 \times 3 \times 2$ (144 atoms) for Li_2O_2, $2 \times 2 \times 3$ (144 atoms) for Na_2O_2, $2 \times 2 \times 2$ (128 atoms) for K_2O_2, and $3 \times 3 \times 2$ (108 atoms) for BaO_2. A plane-wave energy cutoff of 1000 eV was applied in all calculations. We used a Γ-centered $1 \times 1 \times 1$ k-point grid for the Li_2O_2, K_2O_2, and BaO_2 supercells. A Γ-centered $1 \times 1 \times 3$ k-point grid was used for the Na_2O_2 supercell, due to its indirect band gap (see Fig. 2). To form an electron polaron in these materials, an extra electron was added into a given supercell (with a uniform compensating background charge to maintain charge neutrality) and the supercells were then relaxed while keeping their volume and shape fixed. When an extra electron is added into such a supercell, it will reside in two possible configurations. If the symmetry of the lattice is unbroken, the extra electron will be delocalized at the CBM—see Fig. 1(c,i). However, if distortions are added on one of the oxygen dimers the extra electron will self-localize forming a polaron in these materials—see Fig. 1(c,ii). In both the delocalized free electron configuration and the localized polaron configuration the atomic structure was relaxed utilizing HSE06 at the default mixing parameter of 0.25, while keeping the volume and shape fixed.

To compute polaron formation barriers, self-consistent calculations were performed on atomic structures linearly interpolated between the relaxed delocalized and fully formed polaron states. For these barrier calculations we tuned the HSE06 mixing parameter away from 0.25 to satisfy the generalized form of Koopmans' theorem [49–51]. We did not choose to use the climbing image nudged elastic band (CI-NEB) method to compute these polaron formation pathways [55] due to the extremely high computational demand imposed by coupling CI-NEB and HSE06 calculations at ten or more image points. The linearization method should be a fair approximation when computing polaron formation in metal peroxides, since the formation and relaxation pattern are relatively simple—mainly determined by elongation of the oxygen dimer. Additionally, we compared the NEB and linear interpolation approaches via the PBE functional and found that the polaron formation barriers agree reasonably well.

Finally, the software package VESTA [56] was used to visualize crystal structures and band decomposed charge densities; and the element-decomposed band structure was plotted following the approach detailed in Ref. [57].

III. RESULTS

A. Lattice and electronic structures

Experimentally, Li_2O_2 and Na_2O_2 crystallize into a hexagonal structure with respective space groups of: $P6_3/mmc$, $a = 3.142$, $c = 7.65$, 2 formula units [58,59]; and $P\bar{6}2m$, $a = 6.22$, $c = 4.47$, 3 formula units [60,61]. While K_2O_2 has been found to adopt an orthorhombic structure (space group $Cmca$, $a = 6.733$, $b = 6.996$, $c = 6.474$, 4 formula units) [62–64] and BaO_2 a tetragonal structure (space group $I4/mmm$, $a = 3.8114$, $c = 6.8215$, 2 formula units) [65]. Our computed lattice parameters agree well with these experimental values (see the Supplemental Material [52] to this work). In Figs. 2(a,i) through 2(d,i) the lattice structures of these four materials are provided, where it can be seen that the oxygen atoms are paired up in each material. In each case the oxygen dimers accept two electrons from the surrounding metal cations to form peroxide anions. The two oxygen atoms in the peroxide anions are covalently bonded, but if we view the peroxide anions as an integral component we find that they bind ionically to the surrounding metal cations [63,66,67].

The element-projected band structures of these four metal peroxides are provided in Figs. 2(a,ii) through 2(d,ii). Here it can be seen that metal cations have little contribution to the valence band edge and their contributions to the conduction band edge increases progressively from Li_2O_2 through to BaO_2—a metallic ion dominated conduction band is blue, while one dominated by oxygen p orbitals is red. Experimental reports on the electronic structure of Li_2O_2 are very limited and electronic structure insights primarily arise from theoretical computations [68]. Hence, the calculated band gap of Li_2O_2 ranges significantly among the various theoretical calculation methods [69,70]. With our calculated HSE06 mixing parameter of $\alpha = 0.34$ via the generalized Koopmans' theorem, we obtained a band gap 5.4 eV for Li_2O_2. The same approach was applied to obtain the band gaps of the other metal peroxides calculated in this paper (see Table I), for which experimental reports are also very limited.

Let us now consider the oxygen projected density of states (PDOS) of these four materials in Figs. 2(a,iii) through 2(d,iii). Here we can see that the peroxide anions in the

TABLE I. HSE06 Mixing parameter (α), band gap (ε_G), polaron formation barrier height (E_A), and polaron formation energies (ΔE_{POL}) of the peroxides studied

	Li_2O_2	Na_2O_2	K_2O_2	BaO_2
α	0.34	0.37	0.35	0.28
ε_G (eV)	5.4	4.9	4.3	3.9
E_A (eV)	0.007	0.08	0.330	0.402
ΔE_{POL} (eV)	−2.6	−1.9	−1.4	−1.0

solid qualitatively retain much of the character of an isolated oxygen molecule. For comparison, the $2p$ molecular orbitals of an isolated oxygen molecule (lying along z axis) are shown in the inset of Fig. 2(b,iii), which are in the sequence of σ_{2p}, π_{2p}, π^*_{2p}, and σ^*_{2p} [20]. A peroxide anion in these solids accepts two more electrons from the surrounding metal atoms, so a peroxide anion O_2^{2-} contains ten electrons in its $2p$ orbitals. This results in fully occupied σ_{2p}, π_{2p}, and π^*_{2p} molecular orbitals [66]. Hence the upper valence bands of these metal peroxides are mainly composed of the π_{2p} and π^*_{2p} O_2^{2-} molecular orbitals, while the lower valence band is primarily composed of σ_{2p} molecular orbitals. Conversely, the σ^*_{2p} O_2^{2-} molecular orbitals reside in the conduction band but their location within the conduction band varies significantly between the four materials [see Figs. 2(a,iii) through 2(d,iii)].

The contributions from the metal atoms to the CBM differ in each of these metal peroxides, as illustrated by the orbital composition PDOS plots in Figs. 2(a,iv) through 2(d,iv). Here we have plotted the PDOS from the metal cations on the left in blue and PDOS from oxygen p_z orbitals on the right in red. This plotting approach allows us to clearly distinguish the relative contributions of each species to the CBM. In Li_2O_2, the oxygen p_z orbitals dominate the CBM and the s orbitals from Li atoms contribute little [see Fig. 2(a,iv)]. While in Na_2O_2, the cation s orbitals contribute nearly the same as the oxygen p_z orbitals to the conduction band minimum [see Fig. 2(b,iv)]. However, in K_2O_2 and BaO_2 the contributions from the K s orbitals and Ba d orbitals begin to dominate [see Figs. 2(c,iv) and 2(d,iv)]. The role of the cation orbitals is especially strong in BaO_2, where the CBM is comprised completely of Ba d states—shown in Fig. 2(d,iv). Through the course of this study we will demonstrate that this subtle difference near the conduction band minimum has a large impact upon the polaron formation physics.

B. The initial stage of polaron formation and its energetic contributions

The total energy difference between the polaron and free electron configurations is called the polaron formation energy [given as ΔE_{POL} in Fig 1(b)]. Negative polaron formation energies indicate the polaron configuration is more stable than the free electron configuration, which we have found to be the case for each of the four peroxides studied in this work (see Table I). Notably, the polaron formation energies in these metal peroxides are quite large compared with those typically found in transition metal oxides [22,32]. The reported polaron formation energy for Li_2O_2 varies widely between functionals, but they are generally larger than 1 eV [20,67,70] and even the Perdew-Burke-Ernzerhof (PBE) functional has been shown to stabilize an electron polaron in Li_2O_2 [71]. It has been postulated that an electron polaron in Li_2O_2 may stabilize due to the "cleavage" of the O-O bond in the matrix of Li^+ ions [20], drawing parallels with the "bond-breaking" lattice relaxation mechanism reported for *DX* centers in $Al_xGa_{1-x}As$ and GaAs [72]. For all the peroxide polarons studied in this work, we have found that the polaron state [ε_p given in Fig. 1(a)] lies more than 3 eV from the conduction band edge (ε_c) [20,73]. Hence, the polaron trap states are quite deeply bound for all of these peroxides (full PDOS plots are provided in the Supplemental Material [52]). Experimental reports on the polaronic properties of these materials are quite limited, with the most abundant literature coming from studies of Li_2O_2 [74–77].

To compute the polaron formation properties of each peroxide, we linearly interpolated lattice coordinates between the initial delocalized free electron configuration and the final localized polaron configuration. Subsequently, self-consistent N and $N+1$ electron static calculations were run at each interpolated configuration to obtain $E_{\rm POL}$, $E_{\rm LAT}$, and $E_{\rm EL}$ (as discussed in the context of Fig. 1). One may compute the lattice strain penalty $E_{\rm LAT}$ as the total energy difference between the unstrained lattice and polaron strained lattice coordinate computed for N electrons (where the system contains $N+1$ electrons when a polaron is present). Conversely, $E_{\rm POL}$ is computed for the same atomic coordinates but for a system containing $N+1$ electrons. Thus, the electronic energy relaxation is typically extracted as $E_{\rm EL} = E_{\rm POL} - E_{\rm LAT}$ across the entire polaron formation pathway. The values of $E_{\rm POL}$ computed along ten such linearly interpolated coordinates are plotted in Fig. 3(a) with respect to the polaron induced bond length elongation of the oxygen dimer for each peroxide. We used oxygen dimer elongation as a characteristic measure of the polaron formation coordinate in these peroxides, since it is the dominant distortion feature in the formation process. The extension of the O-O bond length is illustrated for Li_2O_2 as an inset to Fig. 3(a); all four peroxides experience a similar polaron distortion.

In Fig. 3(a) we can see that there are two local minima during the formation process: one at the delocalized free electron state (zero elongation) and a second at the fully relaxed small polaron state. The polaron formation energy between these two states ($\Delta E_{\rm POL}$) differs progressively between the four peroxides, with BaO_2 having the smallest formation energy at -1.0 eV and Li_2O_2 the largest at -2.6 eV (see Table I). There is also an energy barrier to polaron formation (E_A) present between the local minima ranging from 0.402 eV in BaO_2 down to 0.007 eV in Li_2O_2 (see Table I). Physically, this barrier represents an activation energy that the system must overcome in order to form a polaron from a free electron state [13]. It is the physical origin of this barrier and its variation between the four peroxides which is the focus of this work.

To this end, in each material we finely sampled $E_{\rm POL}$ at 20 points from the free electron configuration across each barrier to a dimer elongation of 0.25 Å as displayed in Fig. 3(b). At elongations beyond 0.25 Å we found that DFT can produce a spin transition on the polaron site, which further complicates the analysis beyond the main barrier physics (this is discussed in the Supplemental Material [52]). Further separation into the

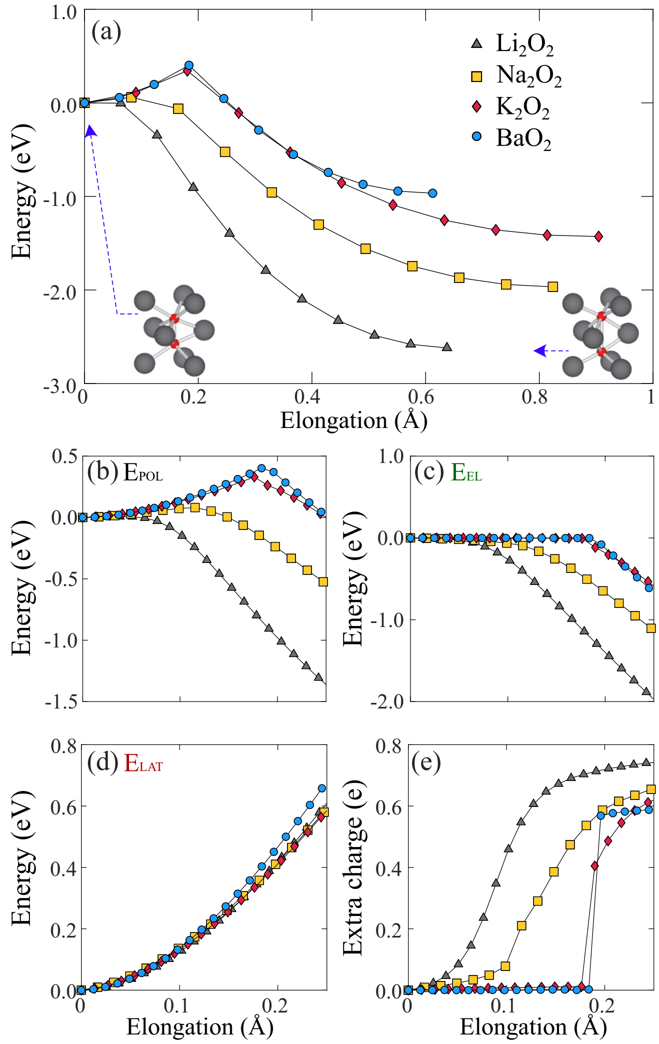

FIG. 3. Polaron formation properties of Li_2O_2, Na_2O_2, K_2O_2, and BaO_2: (a) Formation energy $E_{\rm POL}$ from the free electron configuration to the fully localized configuration; (b) resolved $E_{\rm POL}$ formation energy curve up to 0.25 Å elongation of the oxygen dimer; (c) resolved $E_{\rm EL}$ electronic relaxation energy; (d) resolved lattice strain energy $E_{\rm LAT}$; and (e) resolved charge density localization in each elongated oxygen dimer obtained through a Bader analysis.

$E_{\rm EL}$ and $E_{\rm LAT}$ contributions to the polaron formation barrier are given in Figs. 3(c) and 3(d), respectively. Strikingly, the lattice strain penalty ($E_{\rm LAT}$) is nearly the same in each peroxide [see Fig. 3(d)]. Hence, across the four materials the presence of a barrier is primarily dictated by the behavior of $E_{\rm EL}$ as determined by Eq. (1) and shown in Fig. 3(c). From this we can see that the primary feature determining the height of any such polaron formation barrier is the length to which the oxygen dimer must elongate prior to electronic relaxation occurring (given as approximately x_A in Fig. 1). For example, in Fig. 3(c) we see that BaO_2 and K_2O_2 peroxide dimers must elongate by almost 0.2 Å prior to $E_{\rm EL}$ lowering; while $E_{\rm EL}$ begins to relax almost immediately upon elongation in Li_2O_2 and an intermediate length is found for Na_2O_2 [78]. The physics behind the length of this "electronic relaxation delay" originates from the electronic structure of each material as shall be investigated shortly.

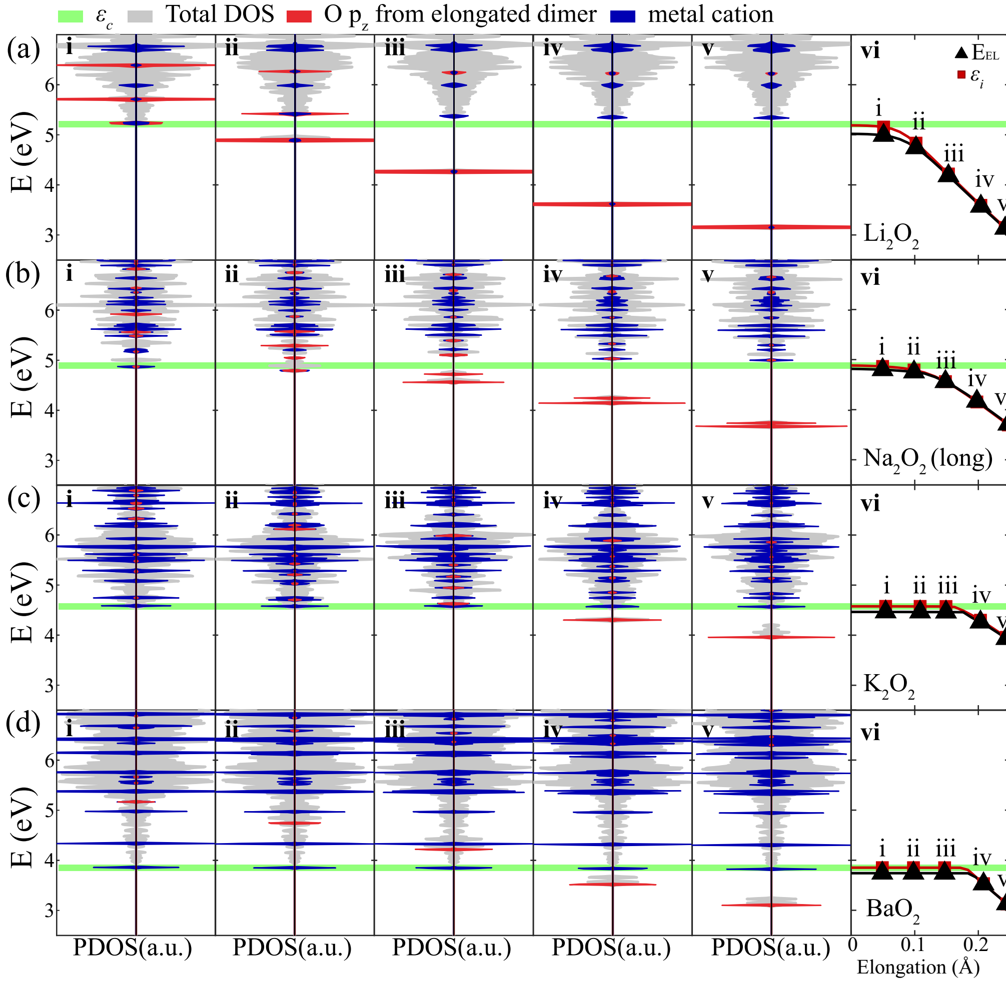

FIG. 4. Conduction band evolution of the spin-polarized projected density states (PDOS) on the p_z orbitals (red) of the elongating of oxygen dimer during polaron formation at distortions of approximately 0.05 Å (i), 0.10 Å (ii), 0.15 Å (iii), 0.20 Å (iv), and 0.25 Å (v). The blue PDOS indicates the *s* orbitals of metal atoms in (a) Li_2O_2, (b) Na_2O_2, (c) K_2O_2, and the *d* orbitals of Ba atoms in (d) BaO_2. The rightmost column (vi) displays E_{EL} in black and the lowest unoccupied single-particle state (ε_i) colored in red. The PDOS in blue and red are self-consistent HSE06 calculations with Γ-centered *k* point for Li_2O_2, K_2O_2, BaO_2 and Γ-centered 1 × 1 × 3 *k*-point grid for Na_2O_2. The background total DOS in gray was computed non-self-consistently with the following *k*-point grid sampling: 5×5×5 for Li_2O_2 and BaO_2, and 3×3×3 for Na_2O_2 and K_2O_2. The conduction band minimum (CBM) is marked in green on all PDOS plots.

It is also instructive to explore the polaron localization physics in each peroxide. This can be accomplished to first order through a Bader analysis [79] of the added electron density on the polaron anchoring oxygen dimer as provided in Fig. 3(e). Here we can see that there is a gradual smooth localization of the electron density in Li_2O_2 and Na_2O_2 as a polaron is formed. However, in K_2O_2 and BaO_2 the added electron localizes much more abruptly near the barrier at a "critical" elongation length near x_A [see Figs. 1(b) and 3(e)]. Hence, the Bader analysis suggests that the ability of charge to localize adiabatically (smoothly) is closely associated with the polaron formation barrier height. Specifically, Fig. 3(e) implies that smooth adiabatic localization is correlated with a low activation barrier and abrupt diabatic localization is correlated with a high activation barrier to polaron formation.

C. Electronic structure evolution during polaron formation

So far we have shown that the electronic relaxation (E_{EL}) delay plays a key role in the determining the presence of a polaron formation barrier—as first pointed out by Mott and Stoneham [29]. To understand the origin of this delay let us now examine the electronic structure changes occurring during polaron formation. This will lead to important insights correlating the degree of hybridization between the eventual polaron state and CBM with the magnitude of the polaron formation barrier. In this regard, it is instructive to examine the PDOS changes that each peroxide material undergoes during the polaron formation process as given in Fig. 4. Due to space limitations, we only selected five of the stages along the formation path traversed by each peroxide in Fig. 4. These stages correspond to oxygen dimer elongations of about 0.05, 0.10, 0.15, 0.20, and 0.25 Å, respectively, and are denoted as images i through v—with one set of images for each peroxide. Note, the PDOS properties at 0.0 Å elongation were given earlier in Fig. 2.

We begin again by considering Li_2O_2 in Fig. 4(a). Here we can see in Fig. 4(a,i) that a small elongation of 0.05 Å immediately results in the p_z orbitals of the polaron centered dimer (shown in red) lowering down to the Li_2O_2 CBM at ε_c (marked in green). Subsequently, further distortion drives the development of a polaronic state below ε_c in Figs. 4(a,ii) through 4(a,v). This transition can be directly mapped by tracking the energetic location of the lowest unoccupied single-particle energy (ε_i) during the polaron formation process as given in Fig. 4(a,vi) and plotted against $E_{\mathrm{EL}} = E(N+1) - E(N)$ (the electronic relaxation energy discussed in the context of Figs. 1 and 3). Note that in order to match the single-particle energies of each PDOS plot in images i through v in Fig. 4, we shifted E_{EL} in image v with respect to the Fermi level of each material. Here we see that the rapid descent of E_{EL} can be directly explained by the strong p_z-orbital hybridization present in the Li_2O_2 CBM [see Fig. 2(a)]. Thus strong hybridization between the orbitals that form the polaron (p_z orbitals in this case) and those of the CBM results in the rapid adiabatic electronic structure relaxation into a polaron configuration and a correspondingly small formation barrier.

Next, we consider the PDOS evolution of Na_2O_2 in Fig. 4(b). After a small elongation of 0.05 Å polaron centered dimer, there is only a little portion of the p_z orbitals of the polaron centered dimer at ε_c [see Fig. 4(b,i)]. The p_z orbitals of the dimer begin to pass ε_c around 0.10 Å elongation [as shown in Fig. 4(b,ii)] and further distortion of the dimer continues to lower the polaron centered p_z orbital. In comparison to Li_2O_2, the oxygen dimer in Na_2O_2 requires a further ∼0.10 Å in distortion to lower the polaron centered p_z orbitals down to ε_c. This can be seen more closely by examining electronic relaxation (E_{EL}) differences between Figs. 4(a,vi) and 4(b,vi). The increased electronic relaxation delay demonstrated for Na_2O_2, which is larger than that found in Li_2O_2, can be understood by noting the reduced p_z-type character of the CBM in Na_2O_2—this is evident upon comparing Figs. 2(a) and 2(b).

Lastly, consider the polaron PDOS evolution of K_2O_2 and BaO_2 together in Figs. 4(c) and 4(d). In the case of K_2O_2 the polaron centered p_z orbital (in red) starts out very weakly hybridizing near the CBM [see Fig. 4(c,i)]. It is only after a significant elongation between 0.15 and 0.20 Å that the polaron begins to localize and pass ε_c [see Figs. 4(c,iii) and 4(c,iv)]. In BaO_2 even weaker hybridization between the polaron p_z-orbital and d-orbital based conduction band results in similarly long delay until ε_c is passed [as shown in Figs. 4(d,i) through 4(d,v)]. Again, this PDOS exhibited delay in the motion of the lowest unoccupied single-particle energy (ε_i) is directly correlated with the electronic relaxation (E_{EL}) delay experienced by the polaron as shown in Figs. 4(c,vi) and 4(d,vi)—see also Fig. 3. Thus, we see that with decreasing CBM hybridization increasingly larger distortions are needed to lower the orbitals of a polaron down below ε_c. This results in the sizable electronic relaxation delay [denoted as x_A in Fig. 1(b)] and increased in activation barriers exhibited by both materials (see Fig. 3). Similarly, the decreased adiabaticity in these materials is a consequence of decreased hybridization of the polaron anchoring p_z orbitals with the CBM.

D. Correlating total energy and single-particle energies in polaron formation barrier calculations

Before wrapping up this portion of our investigation, it is important to understand how one is able to directly correlate the lowest unoccupied single-particle energy (ε_i) with the electronic relaxation energy (E_{EL}) experienced by a polaron (as given in Fig. 4). This is not an accidental feature of the calculations presented but directly follows from satisfying the generalized form of Koopmans' theorem within DFT, which can be expressed compactly as [51]

$$E(N+1) - E(N) = \varepsilon_i. \tag{2}$$

Here ε_i is the lowest unoccupied single-particle energy of the N-electron configuration (lacking an extra electron) and $E(N)$ is its total energy; likewise, $E(N+1)$ is the total energy of the $N+1$ electron configuration (containing the extra electron). The generalized form of Koopmans' theorem is satisfied when linearity of the total energy is preserved with respect to variation in the number of electrons from N to $N+1$ (as it would be for the exact DFT functional) [49–51]. In this work we have carefully tuned the HSE06 mixing parameter α for each material to satisfy this criterion as best as possible. Furthermore, a derivative discontinuity was not introduced at the $E(N)$ electron configuration with respect to following linearity up to $N+1$ electrons [49,50]. Therefore, one is able to maintain "equivalence" between the lowest unoccupied single-particle energy of the N electron configuration (where the polaron would sit) and the highest occupied single-particle energy of the $N+1$ electron configuration (where the polaron does sit) [51].

Hence, by examining the electronic structure of the $E(N)$ electron configuration (as plotted in Fig. 4) one can directly assess how the degree of hybridization between the polaron anchoring p_z oxygen state and the CBM of a given peroxide impacts the electronic relaxation delay (at $\sim x_A$) and the corresponding polaron formation barrier (E_A). Moreover, during our polaron decomposition study in Sec. III B we defined $E_{\mathrm{POL}} = E(N+1)$, $E_{\mathrm{LAT}} = E(N)$, and $E_{\mathrm{POL}} - E_{\mathrm{LAT}} = E_{\mathrm{EL}}$ (see also Fig. 3). This expression is identical to Eq. (2), thus one can make the equivalence $E_{\mathrm{EL}} = \varepsilon_i$ and accurately correlate electronic structure and total energy information. However, due to exchange-correlation errors present in various functionals, this relationship between total energies and single-particle energies cannot be satisfied by an arbitrary DFT functional [49–51] (further examples of this are given in the Supplemental Material [52], also Refs. [80–88] therein). This means that without working to satisfy the generalized form of Koopmans' theorem one cannot necessarily have confidence that single-particle information (e.g., Fig. 4) can be utilized to understand the hybridization physics determining the activation barrier to polaron formation (e.g., Fig. 3). As discussed in Ref. [16], the charge neutral N electron single-particle states are regarded as more accurate in VASP and we have plotted those in Fig. 4.

E. Localization properties near the barrier

We will now further explore how the degree of hybridization between the polaron state (ε_p) and CBM (near ε_c) correlates with the magnitude of the polaron formation barrier. To this end the real-space charge density of the added electron is plotted in Fig. 5 within approximately ±0.025 Å oxygen dimer elongation about the formation barrier maximum of each peroxide—exact image locations are given in Fig. 5. The

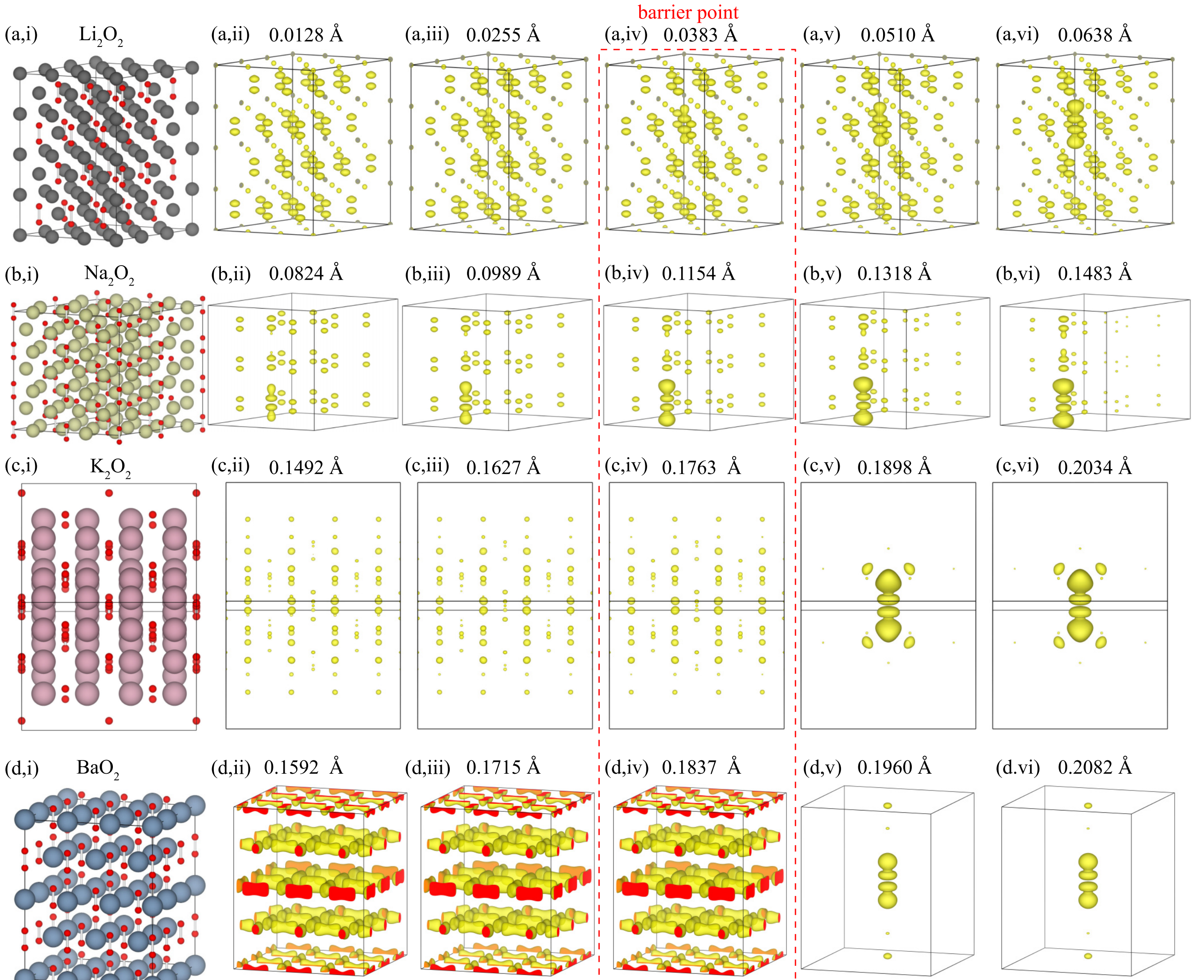

FIG. 5. Band-decomposed charge density of added extra electron at five configurations near the polaron formation barrier point for (a) Li_2O_2, (b) Na_2O_2, (c) K_2O_2, and (d) BaO_2. An isosurface value of $0.001e/\text{Å}^3$ was selected for (a)–(c). To improve visualization, the isosurface value was set to $0.0003e/\text{Å}^3$ for (d,ii) through (d,iv) and $0.003e/\text{Å}^3$ for (d,v) and (d,vi). The red balls represent oxygen atoms. The black, yellow, purple, and blue balls represent Li, Na, K, and Ba, respectively.

resulting analysis in Fig. 5 consists of five closely spaced "snapshots" of the localization transition at and near x_A [the coordinate of the formation barrier maximum given in Fig. 1(b)].

Let us begin by considering the near-barrier localization properties of Li_2O_2 in Figs. 5(a,i) through 5(a,vi). Here we can see that the electron is largely delocalized to the left of the barrier [see Fig. 5(a,ii)] and undergoes a smooth adiabatic localization process as it transitions over the barrier to enter the initial stages of polaron formation. Note we are showing less than 10% of the full polaron distortion, nevertheless we can already see that at just 0.0255 Å past the barrier p_z-type electron localization is already evident [see Fig. 5(a,vi)]. Indeed, one can view this adiabatic polaron formation process [in Figs. 5(a,ii) through 5(a,vi)] as analogous to a "localized lowering" of the CBM, whereby the p_z-type free electron states of the CBM become progressively more trapped in a "local well" formed by the distortion of the oxygen dimer bond on the polaron site.

Next consider the localization physics of Na_2O_2 as presented in Figs. 5(b,i) through 5(b,vi). In this example, localization still proceeds in a primarily adiabatic (smooth) manner but occurs less smoothly than in Li_2O_2 [also indicated by the Bader analysis in Fig. 3(e)]. This is exemplified by the clear appearance of p_z-type localized state only after 0.0824 Å distortion of the oxygen dimer. Both Li_2O_2 and Na_2O_2 display largely adiabatic localization properties, but the transition is more adiabatic in Li_2O_2 and appears less so in Na_2O_2.

Finally, consider the localization properties of K_2O_2 and BaO_2 together. In Figs. 5(c,i) through 5(c,vi) we see that the added electron localizes abruptly in K_2O_2, just after crossing the polaron formation barrier. Even more abrupt localization properties are exhibited by BaO_2 in Figs. 5(d,i) through 5(d,vi). In the case of K_2O_2 we see that the free electron is primarily situated on the K^+ cations before the barrier [in Figs. 5(c,ii)–5(c,iv)], with a slight degree of hybridization on the p_z orbitals of the oxygen dimers, and transitions to strong p_z anchoring in the polaron state after crossing the barrier [in Figs. 5(c,v)–5(c,vi)]. Even more strikingly in BaO_2, we find very weak hybridization between the free electron state and polaron state before and after crossing the barrier maximum at x_A. Just before/at the barrier the free electron state is strongly delocalized and situated entirely on the Ba^+ cations [see Figs. 5(d,ii)–5(d,iv)]. However, immediately after the barrier the electron becomes situated on a p_z anchored polaron orbital directly perpendicular to the free electron wave function prior to the barrier [see Figs. 5(d,v) and 5(d,vi)].

Clearly, in both K_2O_2 and BaO_2 the electron localization transition is largely diabatic in nature and this important physics must be closely correlated with the presence and enhanced magnitude of the polaron formation barrier found in K_2O_2 and BaO_2 (see Fig. 3). Conversely, the reduced polaron formation barriers obtained in Li_2O_2 and Na_2O_2 indicate that a reduced formation barrier is correlated with the decreased degree of adiabaticity present. The origin of these adiabaticity trends can be understood by returning to Figs. 2 and 4.

Beginning with Li_2O_2 in Figs. 2(a,ii) through 2(a,iv) it can be seen that the bottom of the conduction band is strongly dominated by oxygen p orbitals. Hence, the distortion of an oxygen dimer (and its p orbitals) immediately impacts upon the local electronic structure of the lowest unoccupied eigenstate [i.e., the CBM as shown in Fig. 4(a)] and results in a low adiabatic barrier to polaron formation (see Table I and Fig. 3). However, the adiabaticity trend beings to decline in Figs. 2(b,ii) through 2(b,iv), where the p-orbital character of the Na_2O_2 CBM is less pronounced. Thus, Na_2O_2 in the distortion of the oxygen dimer during polaron formation couples less strongly to the CBM [as shown in Fig. 4(b)] and a larger polaron activation barrier results (see Fig. 3 and Table I). Next, we see that for K_2O_2 in Figs. 2(c,ii) through 2(c,iv) the CBM is heavily dominated by metallic orbitals. Hence, in K_2O_2 an even larger oxygen dimer distortion is needed to draw an electron out of the conduction band and onto a σ^*_{2p}-type localized polaron state on an oxygen dimer [as shown in Fig. 4(c)]. This then results in larger and more diabatic barriers (see Fig. 3). Lastly, consider the electronic structure of BaO_2 in Figs. 2(d,ii) through 2(d,iv). Here a complete decoupling occurs between the oxygen p orbitals, which will anchor the polaron state on an elongated dimer, and the Ba dominated CBM. Therefore an extended dimer distortion is needed in BaO_2 to pull an oxygen σ^*_{2p}-type orbital down enough such that an electron in the CBM begins to localize [as shown in Fig. 4(d)]. This strong separation between the O and Ba conduction band orbitals leads to the pronounced diabaticity that is exhibited in Figs. 5(d) and 3(e). Similarly, on the other extreme the strong p-orbital hybridization of the CBM in Li_2O_2 leads to the marked adiabaticity displayed in Fig. 5(a). While for Na_2O_2 and K_2O_2 we obtain results that are somewhat intermediate between the two extremes [see Figs. 5(b), 5(c), and 3(e)].

IV. DISCUSSION

This work primarily builds off the Mott-Stoneham small polaron formation model (illustrated in Fig. 1) [29]. However, by providing a detailed *ab initio* analysis it differs from the work of Mott and Stoneham in two key respects. First, we explored the degree to which hybridization between polaron orbitals and the conduction band minimum impact upon the physics of polaron formation. Second, the molecular nature of small polaron trapping is more clearly substantiated than the square-well model utilized by Mott and Stoneham. The second point of differentiation is essentially common to all *ab initio* studies of small polarons, so it does not merit much discussion [16–23,37,89]. One might only comment that in a small polaron the quantization physics of energy levels resembles more closely that of small molecules and single atoms (depending on the nature of the localization site), rather than that of a square well—which has been reproduced by many *ab initio* studies [16–23,37,89]. In the peroxides studied, quantization on the polaron site was primarily in the form of the well known O_2 molecular quantum orbitals (σ_{2p}, π_{2p}, π^*_{2p}, and σ^*_{2p} as illustrated in Figs. 2 and 4).

The first point of differentiation, however, constitutes the main contribution of this work and deserves further detailed discussion. Through our *ab initio* study of four metal peroxides, we have shown that the degree of polaron-orbital hybridization with the CBM directly impacts on the magnitude of the polaron formation barrier (and, correspondingly, the electronic relaxation delay x_A). This relationship between the CBM and the polaron formation barrier is summarized in Fig. 6. We hypothesize that this physics is much more universal beyond simply peroxides and constitutes a conceptual framework for understanding small polaron formation barriers.

If a polaron orbital is strongly hybridized with the CBM, then a small lattice perturbation (which locally lowers the CBM) is able to successfully initiate polaron formation and a negligible polaron formation barrier results (that is, $x_A \approx 0$). Both Li_2O_2 and Na_2O_2 are examples of this stronger CBM hybridization scenario, following the physics illustrated in Fig. 6(a). In both Li_2O_2 and Na_2O_2 the σ^*_{2p} orbital, which will eventually anchor the polaron state, is substantially hybridized with the CBM [see Fig. 6(a,i)]. Hence, in Li_2O_2 and Na_2O_2 a localized stretching distortion of the O_2^{2-} dimer rapidly lowers the similarly based σ^*_{2p} CBM (where the free electron is initially located) around the dimer and also leads to a near immediate electronic relaxation (E_{EL}) of polaron orbital into the band gap [see Fig. 6(a,i)]. Thus, when E_{EL} drops nearly immediately with respect to the lattice distortion coordinate (x) we obtain a negligible polaron formation barrier (and x_A value), since $E_{POL} = E_{LAT} + E_{EL}$ [see Fig. 6(a,ii)].

Conversely, if a polaron orbital is weakly hybridized with the CBM, then an extended lattice distortion (x_A) is needed to pull the polaron orbital down to a point where electronic relaxation can begin to transform a free electron state (at ε_C) into a localized polaron state. Both K_2O_2 and BaO_2 are examples of this weak CBM hybridization scenario as illustrated in Fig. 6(b). In both K_2O_2 and BaO_2 the σ^*_{2p} orbital, which will eventually anchor the polaron state, is weakly hybridized with the CBM which is dominated by metal cation orbitals [see

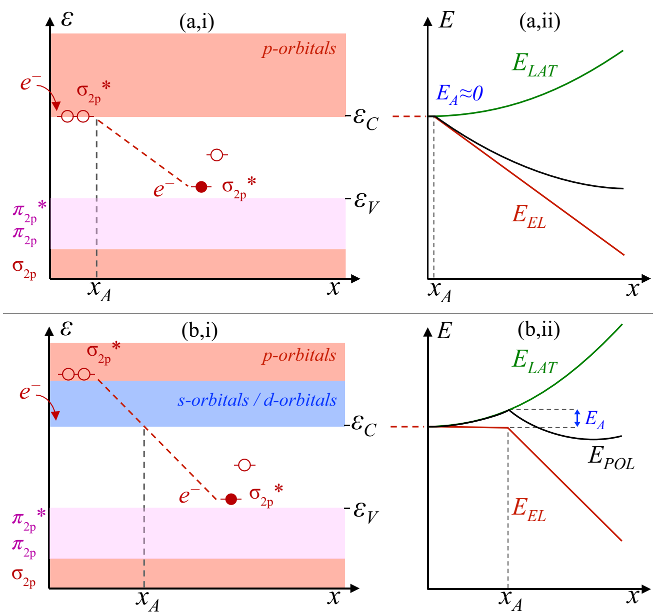

FIG. 6. Primary factors impacting upon the activation barrier (E_A) to polaron formation, illustrated for the model peroxide scenarios explored in this work. (a,i) The electronic structure of a material where the anchoring polaron orbital (in this case a σ^*_{2p} orbital) strongly hybridizes with a CBM (ε_c) composed of p orbitals, and corresponding rapid relaxation of the polaron state into the band gap with respect to the distortion coordinate (x). (b,i) The electronic structure of a material where the anchoring polaron orbital (σ^*_{2p} type) weakly hybridizes with a CBM (ε_c) composed of s orbitals and/or d orbitals, resulting in slow relaxation of the polaron state into the band gap with respect to x. In (a,ii) and (b,ii) we see that E_A maximizes at x_A where the polaron state crosses ε_c into the band gap.

Fig. 6(b,i)]. Hence, in both materials an extended localized distortion of the eventual O_2^{2-} polaron dimer is needed to pull down the σ^*_{2p} polaron anchoring orbital past the CBM where the free electron is initially located [see Fig. 6(b,i)]. Since the electron resides at the CBM for an extended portion of the polaron distortion (x), until the σ^*_{2p} polaron anchoring orbital is drawn past it into the band gap, an extended delay in the electronic relaxation (E_{EL}) occurs. When E_{EL} does not drop until an extended lattice distortion coordinate of x_A is reached, we obtain a correspondingly large polaron formation barrier since $E_{\mathrm{POL}} = E_{\mathrm{LAT}} + E_{\mathrm{EL}}$ [see Fig. 6(b,ii)].

Interestingly, this work was also able to demonstrate that a small polaron formation barrier is associated with an adiabatic transition from the CBM to the polaron state. This was demonstrated for both Li_2O_2 and Na_2O_2 in Figs. 5(a) and 5(b), respectively [see also Fig. 3(e)]. Since small formation barriers arise from polaron states that are strongly hybridized with the CBM, it makes sense that the transition should be adiabatic between the free and localized state. Conversely, it was also demonstrated that a large polaron formation barrier is associated with a more nonadiabatic (diabatic) transition from the CBM to the polaron state. This was demonstrated for both K_2O_2 and BaO_2 in Figs. 5(c) and 5(d), respectively [again, see also Fig. 3(e)]. When a polaron anchoring state is weakly hybridized with CBM, it follows that the transition from the CBM to the polaron state should occur more diabatically when the polaron anchoring state passes the CBM. Alternately, one may view the diabatic scenario as occurring when the polaron state must cross many eigenstates in the conduction band before entering the band gap [see Fig. 6(b,i)]. Conversely, the adiabatic scenario may be characterized by immediate relaxation of the polaron state into the band gap [see Fig. 6(a,i)]. Again, we hypothesize that this adiabaticity physics holds more generally across a wider range of materials.

The most extreme example of diabatic polaron formation was provided by BaO_2. Here the CBM has an entirely Ba d-orbital type character, while the polaron is anchored on a σ^*_{2p} orbital [see Figs. 3(e) and 5(d)]. Indeed, polaron formation in BaO_2 is further intriguing given that its conduction band effective mass is rather light ($m^*_e = 0.46m_e$, where m_e is the free electron mass) as plotted in Fig. 2. Generally, light effective mass materials do not form small polarons [13], which makes sense if one only considers electron-phonon interactions near the CBM. However, BaO_2 demonstrates that higher level states (very weakly hybridized with the CBM) can be lowered to an extent that polarons are formed (as discussed earlier). We have further established this preferred polaron formation mechanism in BaO_2 through molecular dynamics calculations [90,91] (see the Supplemental Material [52]). It is plausible that other materials with a light effective mass might also form small polarons through such a mechanism. However, the stabilization of electron polarons in BaO_2 is mainly due to the "cleavage" of the O_2 dimer (which elongates around 50% as discussed earlier in Sec. III B). Typical polaron distortions are often much smaller, so it is difficult to currently ascertain whether such a large formation barrier might be present in many more materials [32]. For example, when an electron polaron forms on Ti atoms in rutile TiO_2 the nearest O atoms slightly relax outward less than 5% [37]. We shall leave a more expansive investigation of this physics across more materials for future work.

V. CONCLUSION

In this study we have provided *ab initio* insights into the physical nature of polaron formation. Through a comprehensive analysis of four peroxides, serving as a model material family, it was demonstrated that polaron hybridization with the CBM plays a significant role in determining the magnitude of a polaron formation barrier. Polarons which were strongly hybridized with the CBM displayed a smaller adiabatic polaron formation barrier, while polarons which were weakly hybridized with the CBM exhibited a much larger nonadiabatic (diabatic) formation barrier. Moreover, by carefully satisfying the generalized form of Koopmans' theorem in all such calculations, the degree of hybridization was directly correlated with the electronic relaxation delay first postulated by Mott and Stoneham [29]. Only by satisfying the generalized form of Koopmans' theorem can a direct link be drawn between the total energy and single-particle polaron formation pictures. These findings should also prove useful in studying charge localization processes in related material systems [32,33,92]. In general, the findings provided by this work are intended to aid the functional design of polaron properties within electronic and energy materials. For example, increasing the barrier to polaron formation may improve the free electron conductivity of such materials (especially in oxide thin films/coatings).

ACKNOWLEDGMENTS

The authors thank A. Shluger for useful discussions on polaron trapping. S.Y. thanks Y. W. Foong for some stimulating discussions on materials selection. S.Y., Z.W., and K.H.B. acknowledge financial support from NSERC of Canada, FQRNT of Québec, and Hydro-Québec. S.Y. further acknowledges support from the McGill Engineering Doctoral Awards program. M.L.F.B. acknowledges financial support from DAAD of Germany and Mitacs of Canada. Computational for this work was provided by Compute Canada and Calcul Québec.

[1] M. Reticcioli, U. Diebold, G. Kresse, and C. Franchini, Small polarons in transition metal oxides, in *Handbook of Materials Modeling: Applications: Current and Emerging Materials*, edited by W. Andreoni and S. Yip (Springer International Publishing, Cham, 2019), pp. 1–39.

[2] A. J. Rettie, W. D. Chemelewski, D. Emin, and C. B. Mullins, J. Phys. Chem. Lett. **7**, 471 (2016).

[3] T. Berger, M. Sterrer, O. Diwald, E. Knözinger, D. Panayotov, T. L. Thompson, and J. T. Yates, J. Phys. Chem. B **109**, 6061 (2005).

[4] B. Ellis, L. K. Perry, D. H. Ryan, and L. F. Nazar, J. Am. Chem. Soc. **128**, 11416 (2006).

[5] C. M. Yim, M. B. Watkins, M. J. Wolf, C. L. Pang, K. Hermansson, and G. Thornton, Phys. Rev. Lett. **117**, 116402 (2016).

[6] A. Sugita, T. Saito, H. Kano, M. Yamashita, and T. Kobayashi, Phys. Rev. Lett. **86**, 2158 (2001).

[7] M. Ziwritsch, S. Müller, H. Hempel, T. Unold, F. F. Abdi, R. Van De Krol, D. Friedrich, and R. Eichberger, ACS Energy Lett. **1**, 888 (2016).

[8] L. D. Landau, Phys. Z. Sowjetunion **3**, 664 (1933).

[9] S. I. Pekar, Zh. Eksp. Teor. Fiz. **16**, 341 (1946).

[10] E. I. Rashba, Opt. Spektrosk. **2**, 568 (1957).

[11] E. Rashba, Reminiscences of the early days of polaron theory, in *Polarons in Advanced Materials* (Springer, Berlin, 2007), pp. XI–XIV.

[12] A. L. Shluger and A. M. Stoneham, J. Phys.: Condens. Matter **5**, 3049 (1993).

[13] D. Emin, *Polarons* (Cambridge University Press, Cambridge, 2013).

[14] H. Böttger and V. V. Bryksin, *Hopping Conduction in Solids* (Akademie, Berlin, 1985).

[15] P. Erhart, A. Klein, D. Åberg, and B. Sadigh, Phys. Rev. B **90**, 035204 (2014).

[16] P. Deák, B. Aradi, and T. Frauenheim, Phys. Rev. B **83**, 155207 (2011).

[17] K. E. Kweon, G. S. Hwang, J. Kim, S. Kim, and S. Kim, Phys. Chem. Chem. Phys. **17**, 256 (2015).

[18] M. D. Johannes, K. Hoang, J. L. Allen, and K. Gaskell, Phys. Rev. B **85**, 115106 (2012).

[19] S. Lany, Phys. Status Solidi B **248**, 1052 (2011).

[20] J. Kang, Y. S. Jung, S. H. Wei, and A. C. Dillon, Phys. Rev. B **85**, 035210 (2012).

[21] D. Cortecchia, J. Yin, A. Bruno, S. Z. A. Lo, G. G. Gurzadyan, S. Mhaisalkar, J. L. Brédas, and C. Soci, J. Mater. Chem. C **5**, 2771 (2017).

[22] Z. Wang, C. Brock, A. Matt, and K. H. Bevan, Phys. Rev. B **96**, 125150 (2017).

[23] Z. Wang and K. H. Bevan, Phys. Rev. B **93**, 024303 (2016).

[24] W. H. Sio, C. Verdi, S. Poncé, and F. Giustino, Phys. Rev. B **99**, 235139 (2019).

[25] W. H. Sio, C. Verdi, S. Poncé, and F. Giustino, Phys. Rev. Lett. **122**, 246403 (2019).

[26] Y. Toyozawa, J. Appl. Phys. **33**, 340 (1962).

[27] D. Emin, Adv. Phys. **22**, 57 (1973).

[28] D. Emin and T. Holstein, Phys. Rev. Lett. **36**, 323 (1976).

[29] N. F. Mott and A. M. Stoneham, J. Phys. C: Solid State Phys. **10**, 3391 (1977).

[30] L. C. Ku and S. A. Trugman, Phys. Rev. B **75**, 014307 (2007).

[31] V. V. Kabanov and O. Y. Mashtakov, Phys. Rev. B **47**, 6060 (1993).

[32] J. B. Varley, A. Janotti, C. Franchini, and C. G. Van de Walle, Phys. Rev. B **85**, 081109(R) (2012).

[33] P. Gono, J. Wiktor, F. Ambrosio, and A. Pasquarello, ACS Catal. **8**, 5847 (2018).

[34] N.-H. Ge, C. M. Wong, R. L. Lingle, J. D. McNeill, K. J. Gaffney, and C. B. Harris, Science **279**, 202 (1998).

[35] N. H. Ge, C. M. Wong, and C. B. Harris, Acc. Chem. Res. **33**, 111 (2000).

[36] L. M. Carneiro, S. K. Cushing, C. Liu, Y. Su, P. Yang, A. P. Alivisatos, and S. R. Leone, Nat. Mater. **16**, 819 (2017).

[37] A. Janotti, C. Franchini, J. B. Varley, G. Kresse, and C. G. Van de Walle, Phys. Status Solidi RRL **7**, 199 (2013).

[38] M. Setvin, C. Franchini, X. Hao, M. Schmid, A. Janotti, M. Kaltak, C. G. Van de Walle, G. Kresse, and U. Diebold, Phys. Rev. Lett. **113**, 086402 (2014).

[39] L. Sun, X. Huang, L. Wang, and A. Janotti, Phys. Rev. B **95**, 245101 (2017).

[40] G. Kresse and J. Furthmüller, Phys. Rev. B **54**, 11169 (1996).

[41] G. Kresse and J. Furthmüller, Comput. Mater. Sci. **6**, 15 (1996).

[42] G. Kresse and J. Hafner, Phys. Rev. B **49**, 14251 (1994).

[43] G. Kresse and J. Hafner, Phys. Rev. B **47**, 558 (1993).

[44] J. Paier, M. Marsman, K. Hummer, G. Kresse, I. C. Gerber, and J. G. Angyán, J. Chem. Phys. **124**, 154709 (2006).

[45] J. Heyd, G. E. Scuseria, and M. Ernzerhof, J. Chem. Phys. **118**, 8207 (2003).

[46] G. Kresse and D. Joubert, Phys. Rev. B **59**, 1758 (1999).

[47] P. E. Blöchl, Phys. Rev. B **50**, 17953 (1994).

[48] A. Jain, S. P. Ong, G. Hautier, W. Chen, W. D. Richards, S. Dacek, S. Cholia, D. Gunter, D. Skinner, G. Ceder, and K. A. Persson, APL Mater. **1**, 011002 (2013).

[49] J. P. Perdew, R. G. Parr, M. Levy, and J. L. J. Balduz, Phys. Rev. Lett. **49**, 1691 (1982).

[50] J. F. Janak, Phys. Rev. B **18**, 7165 (1978).

[51] S. Lany and A. Zunger, Phys. Rev. B **80**, 085202 (2009).

[52] See Supplemental Material at http://link.aps.org/supplemental/10.1103/PhysRevB.100.205201 for the computed lattice parameters, polaron PDOS, calculation details regarding the

HSE06 mixing parameter, a discussion on the polaron site spin transition issue, a discussion on image charge corrections, *ab initio* molecular dynamics calculations of BaO_2, and different polaron formation properties from the two sets of bond lengths in Na_2O_2.
[53] See the VASP manual, accurate dos and band-structure calculations.
[54] W. Setyawan and S. Curtarolo, Comput. Mater. Sci. **49**, 299 (2010).
[55] G. Henkelman, B. P. Uberuaga, and H. Jónsson, J. Chem. Phys. **113**, 9901 (2000).
[56] K. Momma and F. Izumi, J. Appl. Crystallogr. **44**, 1272 (2011).
[57] S. P. Ong, W. D. Richards, A. Jain, G. Hautier, M. Kocher, S. Cholia, D. Gunter, V. L. Chevrier, K. A. Persson, and G. Ceder, Comput. Mater. Sci. **68**, 314 (2013).
[58] H. Föppl, ZAAC J. Inorg. Gen. Chem. **291**, 12 (1957).
[59] L. G. Cota and P. De La Mora, Acta Crystallogr. Sect. B **61**, 133 (2005).
[60] R. L. Tallman, J. L. Margrave, and S. W. Bailey, J. Am. Chem. Soc. **79**, 2979 (1957).
[61] S. Yang and D. J. Siegel, Chem. Mater. **27**, 3852 (2015).
[62] T. Bremm and M. Jansen, Z. Anorg. Allg. Chem. **610**, 64 (1992).
[63] A. K. Nandy, P. Mahadevan, and D. D. Sarma, Mol. Simul. **38**, 1308 (2012).
[64] D. V. Korabel'Nikov, Y. N. Zhuravlev, and M. V. Aleinikova, J. Struct. Chem. **53**, 639 (2012).
[65] W. Wong-Ng and R. S. Roth, Phys. C Supercond. Appl. **233**, 97 (1994).
[66] A. K. Nandy, P. Mahadevan, and D. D. Sarma, Phys. Rev. B **84**, 035116 (2011).
[67] J. M. Garcia-Lastra, J. S. Myrdal, R. Christensen, K. S. Thygesen, and T. Vegge, J. Phys. Chem. C **117**, 5568 (2013).
[68] W. Dai, X. Cui, Y. Zhou, Y. Zhao, L. Wang, L. Peng, and W. Chen, Small Methods **3**, 1800358 (2019).
[69] J. S. Hummelshøj, J. Blomqvist, S. Datta, T. Vegge, J. Rossmeisl, K. S. Thygesen, A. C. Luntz, K. W. Jacobsen, and J. K. Nørskov, J. Chem. Phys. **132**, 071101 (2010).
[70] M. D. Radin and D. J. Siegel, Energy Environ. Sci. **6**, 2370 (2013).
[71] Z. Feng, V. Timoshevskii, A. Mauger, C. M. Julien, K. H. Bevan, and K. Zaghib, Phys. Rev. B **88**, 184302 (2013).
[72] D. J. Chadi and K. J. Chang, Phys. Rev. Lett. **61**, 873 (1988).
[73] R. B. Araujo, S. Chakraborty, and R. Ahuja, Phys. Chem. Chem. Phys. **17**, 8203 (2015).
[74] J. Højberg, B. D. McCloskey, J. Hjelm, T. Vegge, K. Johansen, P. Norby, and A. C. Luntz, ACS Appl. Mater. Interfaces **7**, 4039 (2015).
[75] A. C. Luntz, V. Viswanathan, J. Voss, J. B. Varley, J. K. Nørskov, R. Scheffler, and A. Speidel, J. Phys. Chem. Lett. **4**, 3494 (2013).
[76] M. D. Radin, C. W. Monroe, and D. J. Siegel, J. Phys. Chem. Lett. **6**, 3017 (2015).
[77] O. Gerbig, R. Merkle, and J. Maier, Adv. Mater. **25**, 3129 (2013).
[78] In the Supplemental Material it is shown that there are actually two possible polaron formation states for sodium peroxide, a longer dimer and a shorter dimer. In the main part of the paper we discuss the longer dimer. The shorter dimer has a larger activation barrier.
[79] W. Tang, E. Sanville, and G. Henkelman, J. Phys.: Condens. Matter **21**, 084204 (2009).
[80] I. Dabo, A. Ferretti, and N. Marzari, *First Principles Approaches to Spectroscopic Properties of Complex Materials*, edited by C. Di Valentin, S. Botti, and M. Cococcioni (Springer, Berlin, Heidelberg, 2014), pp. 193–233.
[81] A. J. Cohen, P. Mori-Sánchez, and W. Yang, Science **321**, 792 (2008).
[82] S. Lany and A. Zunger, Phys. Rev. B **78**, 235104 (2008).
[83] A. Lindman, P. Erhart, and G. Wahnström, Phys. Rev. B **94**, 075204 (2016).
[84] V. Vlček, H. R. Eisenberg, G. Steinle-Neumann, L. Kronik, and R. Baer, J. Chem. Phys. **142**, 034107 (2015).
[85] L. Zhao, B. Magyari-Köpe, and Y. Nishi, Phys. Rev. B **95**, 054104 (2017).
[86] A. R. Elmaslmane, M. B. Watkins, and K. P. McKenna, J. Chem. Theory Comput. **14**, 3740 (2018).
[87] See the VASP manual, monopole dipole and quadrupole corrections.
[88] G. Makov and M. C. Payne, Phys. Rev. B **51**, 4014 (1995).
[89] T. Maxisch, F. Zhou, and G. Ceder, Phys. Rev. B **73**, 104301 (2006).
[90] S. Nosé, Mol. Phys. **52**, 255 (1984).
[91] J. P. Perdew, K. Burke, and M. Ernzerhof, Phys. Rev. Lett. **77**, 3865 (1996).
[92] S. Lany, J. Phys.: Condens. Matter **27**, 283203 (2015).